GRAVITATIONAL WAVES FROM THREE-DIMENSIONAL CORE COLLAPSE SUPERNOVA SIMULATIONS

H. ANDRESEN, E. MÜLLER, H.T. JANKA.
Max Planck Institut für Astrophysik, Karl-Schwarzschild-Str. 1
85748 Garching, Germany

In this work we present the gravitational wave signals from sophisticated three-dimensional supernova core collapse simulations of three progenitors, of 11.2, 20 and 27 solar masses. In the two most massive models large scale shock deformationw develops. This is reflected in the gravitational wave signals as a strong emission component below ~ 250 Hz.

1 Introduction

Exactly how a core-collapse supernova comes about is still shrouded in mystery. The prevailing theory is the delayed neutrino explosion mechanism[1]: A shock wave form when the contracting iron core reaches nuclear densities and the equation of state stiffens. This halts the collapse and infalling stellar matter bounces off the proto-neutron star(PNS). As the shock wave propagates outwards, through the dense stellar matter, it looses energy and stalls after some hundreds of kilometres. The energy needed to revive the shock wave, ensuring a successful explosions, is thought to be provided by neutrinos streaming out of the PNS. Neutrinos captured in post-shock matter deposit energy. After $\sim$ 100 milliseconds(ms) neutrino heating can be sufficient to revive the shock and successfully launch the supernova. Hydrodynamical instabilities operating behind the stalled shock front have been found to be crucial for the success of this scenario, in particular large scale convection in the neutrino heated post-shock region and the standing accretion shock instability(SASI). See for example Ott[2] for a review of the history of the subject.

Presently we are withnessing the emergence of exploding stars in 3D modelling. Melson *et al*[3] present a successful 3D simulation of a neutrino driven supernova explosion, for a 9.6 $M_{\odot}$progenitor. Observations of a supernova core could compliment the theoretical work and provide much needed insight about the explosion mechanism. Unfortunately in the electromagnetic regime the core is quite literally shrouded by the surrounding stellar material. Gravitational waves(GW) and neutrinos, however, propagate unhindered trough the outer layers of the star and can provide us with direct observations of the core. Here we present the GW arising of the three first 3D core-collapse simulations with sophisticated neutrino physics. The two most massive progenitors(27 and 20 $M_{\odot}$) develop SASI activity, while the third and least massive star(11.2 $M_{\odot}$) show now signs of SASI activity.

2 Numerical set-up

Our analysis is based on 3D simulations of three solar metallicity progenitors with masses $27M_{\odot}$, $20M_{\odot}$ and $11.2M_{\odot}$. These models have been evolved until the onset of iron core collapse[4,5]. Then the 3D core collapses were simulatioed with PROMETHEUS-VERTEX, a hydro code including

the neutrino transport module VERTEX. PROMETHEUS [6] implements a dimensionally split piecewise parabolic method [7] and VERTEX is a "ray-by-ray-plus" neutrino transport module. VERTEX[8] solves the neutrino momentum, energy and Boltzmann equations based on a variable Eddington-factor technique. The equation of state is that of Lattimer & Swesty [9] with a nuclear incompressibility K = 220 MeV. We use an initial grid resolution of 400x88x176 grid cells in r, θ and ϕ, respectively. During the simulations grid adjustments were made to maintain sufficient resolution around the PNS surface.

3 Gravitational wave extraction

In order to extract the GW signal from the hydrodynamical simulations a post-processing step is necessary. A concise description of the formalism used to determine the GW signal arising from matter flow is given below [10].

When expressing the gravitational radiation as a multi-pole expansion one finds that the leading term is given by the quadrupole, this is a consequence of mass and momentum conservation. In the transverse traceless(TT) gauge the gravitational quadrupole radiation tensor, at a distance D from the source, is given by,

$$\boldsymbol{h}^{TT}(\boldsymbol{X},t) = \frac{1}{D}\left[A_{+}\boldsymbol{e}_{+} + A_{\times}\boldsymbol{e}_{\times}\right]. \tag{1}$$

Here $\mathbf{e}_{\times}$ and $\mathbf{e}_{+}$ are the unit linear-polarization tensor given by

$$\boldsymbol{e}_{+} = \boldsymbol{e}_{\theta}\otimes\boldsymbol{e}_{\theta} - \boldsymbol{e}_{\phi}\otimes\boldsymbol{e}_{\phi}, \tag{2}$$

$$\boldsymbol{e}_{\times} = \boldsymbol{e}_{\theta}\otimes\boldsymbol{e}_{\phi} + \boldsymbol{e}_{\phi}\otimes\boldsymbol{e}_{\theta}. \tag{3}$$

$\boldsymbol{e}_{\theta}$ and $\boldsymbol{e}_{\phi}$ are the unit polarization vectors in spherical coordinates. $A_{\times}$ and A_{+} are the two independent wave amplitudes of the TT gauge, given in the slow-motion limit by

$$A_{+} = \ddot{Q}_{\theta\theta} - \ddot{Q}_{\phi\phi}, \tag{4}$$

$$A_{\times} = 2\ddot{Q}_{\theta\phi}. \tag{5}$$

Here $\ddot{Q}$ is second time derivative of the symmetric trace-free(STF) mass quadrupole tensor [11]. In Cartesian coordinates this quantity can be written as,

$$\ddot{Q}_{ij} = \mathrm{STF}\left[\frac{G}{c^4}\int \mathrm{d}^3x\left(v_i v_j - x_i\partial_j\Phi\right)\right]. \tag{6}$$

Here G is Newtons gravitational constant, c the speed of light, v_i and x_i refer to the Cartesian velocity and position ($i = 1, 2, 3$), respectively. The gravitational potential, Φ, refers to the gravitational potential with post-Newtonian corrections taken into account. The advantage of this form is that the second-order time derivatives are transformed in to first-order spatial derivatives, thus circumventing problems associated with the numerical evaluation of second-order time derivatives. Using standard coordinate transformations, between Cartesian and spherical coordinates, we find

$$\begin{aligned}\ddot{Q}_{\theta\phi} = &\left(\ddot{Q}_{22} - \ddot{Q}_{11}\right)\cos\theta\sin\phi\cos\phi \\ &+ \ddot{Q}_{12}\cos\theta\left(\cos^2\phi - \sin^2\phi\right) \\ &+ \ddot{Q}_{13}\sin\theta\sin\phi - \ddot{Q}_{23}\sin\theta\cos\phi,\end{aligned} \tag{7}$$

$$\ddot{Q}_{\phi\phi} = \ddot{Q}_{11}\sin^2\phi + \ddot{Q}_{22}\cos^2\phi - 2\ddot{Q}_{12}\sin\phi\cos\phi \tag{8}$$

and

$$\ddot{Q}_{\theta\theta} = \left(\ddot{Q}_{11}\cos^2\phi + \ddot{Q}_{22}\sin^2\phi + 2\ddot{Q}_{12}\sin\phi\cos\phi\right)\cos^2\theta + \ddot{Q}_{33}\sin^2\theta - 2\left(\ddot{Q}_{13}\cos\phi + \ddot{Q}_{23}\sin\phi\right)\sin\theta\cos\theta. \tag{9}$$

4 Signal description

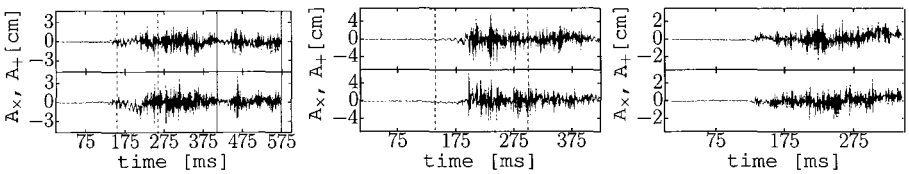

Figure 1 – GW amplitudes as seen by an observer at the pole, normalized by the distance to the source. Left, middle and right panel: 27, 20 and 11.2 $M_\odot$. The top and bottom row represents the cross and plus polarized amplitudes, respectivly. Vertical lines indicate periodes with SASI activity.

Amplitudes for GW generated by asymmetric mass motions are shown in Figure 1. For each progenitor we show two panels representing the cross and plus polarization. The waveforms are in general characterised by an initial quiescent phase, which is followed by a rather stochastic phase with amplitudes of a few cm. Besides from the fact that we see slightly stronger amplitudes in the 27 and 20 $M_\odot$models there is little apparent difference in the waveforms, between the models with and without SASI activity. In order to dissect the signal further we apply the standard Short-time Fourier transform(STFT) to our waveforms. We calculate the STFT for the cross and plus polarization separately before adding them together. Using a time window of 50 ms and shift it 5 ms forward in time each iteration, the resulting spectrograms are shown in Figure 2. Inspecting the spectrograms it is clear that the 11.2 $M_\odot$model stands out, lacking the strong emission below 250 Hz seen in the two SASI models. One can also clearly see that this signal component varies greatly between the 20 and 27 $M_\odot$model. In the former we see a broad and noisy emission component, while we see a clean and narrow emission band in the signal from the more massive progenitor. Common to both models is the fact that the low frequency emission is strongest during the SASI episodes and that the signal is weak after the SASI has died out. A second component of the signal has frequencies above 350 Hz. While this

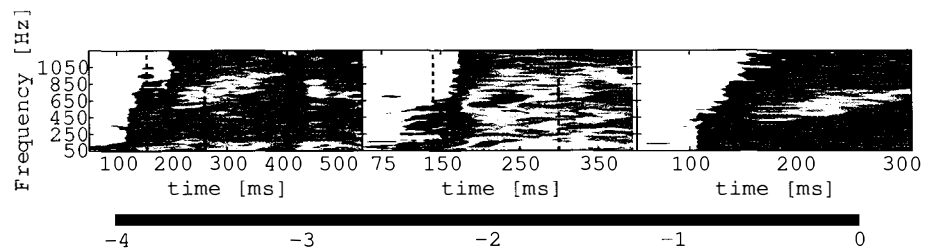

Figure 2 – Normalized spectrogram, summed over the two polarization modes $(|\mathcal{F}(h_+)|^2 + |\mathcal{F}(h_\times)|^2)$. From left to right: the 27, 20 and 11.2 $M_\odot$ model. Colours in log scale. All plots have been normalized by the same factor. Vertical lines indicate periodes with SASI activity.

component is present in all models, it varies strongly from model to model. The 20 $M_\odot$model initially emits in a broad frequency range. As time passes the model slowly develops a narrow emission band. In contrast the more massive 27 $M_\odot$model radiates high frequency GWs in a thin strip. Similarly the 11.2 $M_\odot$progenitor produces a narrow high frequency emission band. In all three models the peak-frequency of this component increases linearly with time.

Acknowledgments

This project was supported by the SFB/TR 7 "Gravitational Wave Astronomy" and ERC-AdG No. 341157-COCO2CASA. The simulations this work is based on could only be achieved with the assistance of high performance computing resources (Tier-0) provided by PRACE on CURIE TN (GENCI@CEA, France) and SuperMUC (GCS@LRZ, Germany).

References

1. H.-T. Janka. Explosion Mechanisms of Core-Collapse Supernovae. *Annual Review of Nuclear and Particle Science*, 62:407–451, November 2012.
2. C. D Ott. TOPICAL REVIEW: The gravitational-wave signature of core-collapse supernovae. *Classical and Quantum Gravity*, 26(6):063001, March 2009.
3. T. Melson, H.-T. Janka, and A. Marek. Neutrino-driven Supernova of a Low-mass Iron-core Progenitor Boosted by Three-dimensional Turbulent Convection. *ApJL*, 801:L24, March 2015.
4. S. E. Woosley and A. Heger. Nucleosynthesis and remnants in massive stars of solar metallicity. *Phys. Rep.*, 442:269–283, April 2007.
5. S. E. Woosley, A. Heger, and T. A. Weaver. The evolution and explosion of massive stars. *Reviews of Modern Physics*, 74:1015–1071, November 2002.
6. B. A Fryxell, E. Müller, and D. Arnett. Preprint0. *Max-Planck-Institut für Astrophysik*, 449, 1989.
7. P. Colella and P. R. Woodward. The Piecewise Parabolic Method (PPM) for Gas-Dynamical Simulations. *Journal of Computational Physics*, 54:174–201, September 1984.
8. M. Rampp and H.-T. Janka. Radiation hydrodynamics with neutrinos. Variable Eddington factor method for core-collapse supernova simulations. *A&A*, 396:361–392, December 2002.
9. J. M. Lattimer and F. D Swesty. A generalized equation of state for hot, dense matter. *Nuclear Physics A*, 535:331–376, December 1991.
10. Müller, E., H.-T. Janka, and A. Wongwathanarat. Parametrized 3D models of neutrino-driven supernova explosions. Neutrino emission asymmetries and gravitational-wave signals. *A&A*, 537:A63, January 2012.
11. L. Blanchet, T. Damour, and G. Schaefer. Post-Newtonian hydrodynamics and post-Newtonian gravitational wave generation for numerical relativity. *MNRAS*, 242:289–305, January 1990.